

# 2D Conjugated Metal–Organic Frameworks Embedded with Iodine for High-Performance Ammonium-Ion Hybrid Supercapacitors

Mingming Gao, Zhiyong Wang, Zaichun Liu, Ying Huang, Faxing Wang, Mingchao Wang, Sheng Yang, Junke Li, Jinxin Liu, Haoyuan Qi, Panpan Zhang,\* Xing Lu,\* and Xinliang Feng\*

Ammonium ions ( $\text{NH}_4^+$ ) are emerging non-metallic charge carriers for advanced electrochemical energy storage devices, due to their low cost, elemental abundance, and environmental benignity. However, finding suitable electrode materials to achieve rapid diffusion kinetics for  $\text{NH}_4^+$  storage remains a great challenge. Herein, a 2D conjugated metal–organic framework (2D *c*-MOF) for immobilizing iodine, as a high-performance cathode material for  $\text{NH}_4^+$  hybrid supercapacitors, is reported. Cu-HHB (HHB = hexahydroxybenzene) MOF embedded with iodine (Cu-HHB/ $\text{I}_2$ ) features excellent electrical conductivity, highly porous structure, and rich accessible active sites of copper-*bis*(dihydroxy) ( $\text{Cu}-\text{O}_4$ ) and iodide species, resulting in a remarkable areal capacitance of  $111.7 \text{ mF cm}^{-2}$  at  $0.4 \text{ mA cm}^{-2}$ . Experimental results and theoretical calculations indicate that the  $\text{Cu}-\text{O}_4$  species in Cu-HHB play a critical role in binding polyiodide and suppressing its dissolution, as well as contributing to a large pseudocapacitance with adsorbed iodide. In combination with a porous MXene anode, the full  $\text{NH}_4^+$  hybrid supercapacitors deliver an excellent energy density of  $31.5 \text{ mWh cm}^{-2}$  and long-term cycling stability with 89.5% capacitance retention after 10 000 cycles, superior to those of the state-of-the-art  $\text{NH}_4^+$  hybrid supercapacitors. This study sheds light on the material design for  $\text{NH}_4^+$  storage, enabling the development of novel high-performance energy storage devices.

## 1. Introduction

Advanced supercapacitors (SCs) exhibit a great application prospect for energy storage due to their high peak power density, fast charge/discharge capability, and long cycling lifetime.<sup>[1]</sup> However, the low energy density of SCs is a commonplace bottleneck, which has been usually addressed by assembling hybrid supercapacitors (HSCs) with a battery-type electrode and a capacitor-type electrode.<sup>[2]</sup> The cationic metallic charge carriers for HSCs include  $\text{Li}^+$ ,  $\text{Na}^+$ ,  $\text{K}^+$ ,  $\text{Mg}^{2+}$ ,  $\text{Zn}^{2+}$ , among others.<sup>[3]</sup> By contrast, non-metallic charge carriers (e.g.,  $\text{H}^+$ ,  $\text{NH}_4^+$ ,  $\text{F}^-$ ,  $\text{Cl}^-$ ) exhibit many outstanding features such as low molar mass, small hydrated ionic sizes, less corrosion side effects, and good sustainability.<sup>[4]</sup> Especially,  $\text{NH}_4^+$  has garnered widespread attention due to its ultralow molar mass ( $18 \text{ g mol}^{-1}$ ), small hydration radius ( $3.31 \text{ \AA}$ ), and sustainable resources.<sup>[5]</sup> Additionally, the high dissociation degree of  $\text{NH}_4^+$  in aqueous


M. Gao, Y. Huang, J. Li, P. Zhang, X. Lu  
State Key Laboratory of Material Processing and Die & Mould Technology  
School of Materials Science and Engineering  
Huazhong University of Science and Technology  
Luoyu Road 1037, Wuhan 430074, China  
E-mail: ppzhang@hust.edu.cn; lux@hust.edu.cn

Z. Wang, F. Wang, M. Wang, S. Yang, J. Liu, X. Feng  
Center for Advancing Electronics Dresden (cfaed) & Faculty of Chemistry  
and Food Chemistry  
Technische Universität Dresden  
Mommsenstrasse 4, 01069 Dresden, Germany  
E-mail: xinliang.feng@tu-dresden.de

Z. Wang, X. Feng  
Department of Synthetic Materials and Functional Devices  
Max Planck Institute of Microstructure Physics  
D-06120 Halle (Saale), Germany

Z. Liu  
Key Laboratory of Energy Thermal Conversion and Control  
of Ministry of Education  
School of Energy and Environment  
Southeast University  
Nanjing 210096, China

Y. Huang  
Key Laboratory of Optoelectronic Devices and Systems of Ministry of  
Education and Guangdong Province  
College of Physics and Optoelectronic Engineering  
Shenzhen University  
Shenzhen 518060, China

 The ORCID identification number(s) for the author(s) of this article can be found under <https://doi.org/10.1002/adma.202305575>

© 2023 The Authors. Advanced Materials published by Wiley-VCH GmbH. This is an open access article under the terms of the Creative Commons Attribution License, which permits use, distribution and reproduction in any medium, provided the original work is properly cited.

DOI: 10.1002/adma.202305575

electrolytes contributes to high ionic conductivity, and its tetrahedral structure enables unique intercalation chemistry, distinguishable from other metal ions.<sup>[6]</sup> These unique features position  $\text{NH}_4^+$  as a promising candidate for high-performance HSCs.

Significant efforts have been devoted to developing suitable electrode materials for  $\text{NH}_4^+$ -based energy storage devices toward large capacity/capacitance and stable cycling performance.<sup>[7]</sup> Currently, five main categories of cathode materials have been developed, including Prussian blue analogs (PBAs:  $\text{CuHCF}$ ,  $\text{Na-FeHCF}$ ,  $\text{FeFe(CN)}_6$ , etc.),<sup>[8]</sup> V-based oxides ( $\text{V}_2\text{O}_5$ ,  $\text{NH}_4\text{V}_4\text{O}_{10}$ , defective  $\text{VO}_2$ , etc.),<sup>[9]</sup> Mn-based compounds ( $\text{MnO}_x$ ),<sup>[4b,10]</sup> sulfide-based composites ( $\text{MoS}_2/\text{PANI}$ ),<sup>[11]</sup> and redox-active polymers/covalent organic frameworks (COFs).<sup>[12]</sup> Cui et al. studied the  $\text{NH}_4^+$  storage behavior of PBAs ( $\text{CuHCF}$  and  $\text{NiHCF}$ ) in 2012,<sup>[13]</sup> initiating the exploration of  $\text{NH}_4^+$  host materials. Then, Gogotsi et al. reported the  $\text{NH}_4^+$  ion storage in MXenes.<sup>[14]</sup> Moreover, the intercalation/deintercalation chemistry of  $\text{NH}_4^+$  has also been demonstrated in other layered materials (e.g.,  $\delta\text{-MnO}_2$ ,  $\text{NH}_4\text{V}_4\text{O}_{10}$ , and Mn-Al layered double hydroxides)<sup>[4b,9a,15]</sup> and redox-active polymers/COFs.<sup>[12]</sup> Despite the above-mentioned progresses, the reported electrode materials generally exhibited insufficient capacity/capacitance and inferior structural stability. Thus, it is highly desirable to explore new cathode materials for reversible  $\text{NH}_4^+$  storage aiming for excellent electrochemical performance.

In this study, we have demonstrated that Cu-HHB (HHB = hexahydroxybenzene) 2D conjugated metal–organic framework (2D *c*-MOF) composited with iodine ( $\text{I}_2$ ) serves as an electroactive cathode material for  $\text{NH}_4^+$  HSCs. The Cu-HHB presents high electrical conductivity, abundant porosity, and rich active sites, providing accessible pseudocapacitive sites and adsorbable polyiodide sites to restrain the dissolution into the electrolyte. Electrochemical kinetics analyses and density functional theory (DFT) calculations verify that copper-*bis*(dihydroxy) ( $\text{Cu-O}_4$ ) species in Cu-HHB serve as both the redox-active sites and binding sites for polyiodide. Accordingly, the as-synthesized Cu-HHB/ $\text{I}_2$  electrode displays a high areal capacitance of  $111.7 \text{ mF cm}^{-2}$  at  $0.4 \text{ mA cm}^{-2}$  and excellent cycling stability with a capacitance retention of 91.0% after 10 000 cycles in  $1 \text{ M (NH}_4)_2\text{SO}_4$  electrolyte. As a proof-of-concept demonstration, the combination of Cu-HHB/ $\text{I}_2$  cathode and porous MXene (P-MXene) anode in  $\text{NH}_4^+$  HSCs affords a considerable energy density of  $31.5 \text{ mWh cm}^{-2}$  and a record-long lifespan with 89.5% capacitance retention over 10 000 cycles, highlighting its enormous potential for the innovative electronic devices.

S. Yang  
Frontiers Science Center for Transformative Molecules  
School of Chemistry and Chemical Engineering  
Shanghai Jiao Tong University  
Shanghai 200240, China

J. Li  
School of Environmental Science and Engineering  
Huazhong University of Science and Technology  
Luoyu Road 1037, Wuhan 430074, China

H. Qi  
Central Facility of Electron Microscopy  
Electron Microscopy Group of Materials Science  
Universität Ulm  
89081 Ulm, Germany

## 2. Results and Discussion

The Cu-HHB was synthesized by a surfactant-assisted solution growth method (Figure S1, Supporting Information).<sup>[16]</sup> The reaction between  $\text{Cu}^{2+}$  and tetrahydroxy-1,4-quinone occurred in the presence of the anionic surfactant sodium dodecyl sulfate. The experimental details are provided in the Supporting Information. As shown in Figure 1a, the calculated unit-cell model structure of Cu-HHB matches well with the AB slipped-parallel stacking, which shows a typical hexagonal crystal lattice at 2D plane with an interlayer spacing of 0.29 nm. According to scanning electron microscopy (SEM) and atomic force microscopy (AFM) images, the Cu-HHB presents a nanosheet-like 2D morphology with an average thickness of  $\approx 5 \text{ nm}$  (Figure 1b; Figures S2 and S3, Supporting Information). In addition, aberration-corrected high-resolution transmission electron microscopy (AC-HRTEM) was performed to resolve the crystal structure of Cu-HHB with near-atomic resolution. Figure 1c shows the highly ordered hexagonal lattice with atomic precision (resolution,  $\approx 2 \text{ \AA}$ ), which is consistent with the structural simulation.

Cu-HHB is an attractive candidate for loading active iodine ( $\text{I}_2$ ) cathode materials in terms of its layered structure, dense metal centers, well-defined pores, and high electrical conductivity. In addition, the exceptional attributes of Cu-HHB, including its high crystallinity, large domain size, and nanoscale thicknesses, are anticipated to create an abundance of exposed surface area between layers, resulting in a highly accessible surface area. The immobilization of monomeric  $\text{I}_2$  on Cu-HHB was carried out by a melting diffusion method.<sup>[17]</sup> When heating to a high temperature,  $\text{I}_2$  sublimed into vapor, which was easily loaded into the porous framework of Cu-HHB due to the interfacial diffusion effect (Figures S4 and S5, Supporting Information). The weight fraction of  $\text{I}_2$  in Cu-HHB/ $\text{I}_2$  was about 28%. The porosity of Cu-HHB before and after  $\text{I}_2$  loading was evaluated by  $\text{N}_2$  adsorption measurement at 77 K (Figure S6, Supporting Information). The results demonstrate that the introduction of  $\text{I}_2$  led to a discernible decrease in the Barrett–Emmett–Teller surface area of Cu-HHB/ $\text{I}_2$ , recording  $276 \text{ m}^2 \text{ g}^{-1}$ , as compared to the initial value of  $352 \text{ m}^2 \text{ g}^{-1}$  for Cu-HHB. This reduction can be attributed to the partial block of pores prompted by  $\text{I}_2$ . However, the main pore size still retains around 1.2 nm, which can be used as the ion transport channels of the electrolyte. As illustrated in Figures 1d,e, the SEM image and corresponding energy-dispersive X-ray spectroscopy (EDX) elemental mappings indicate the homogeneous distribution of elemental iodine in Cu-HHB. To further reveal the crystallinity and chemical stability of Cu-HHB/ $\text{I}_2$ , powder X-ray diffraction (PXRD) patterns were collected and shown in Figure 1f. The Cu-HHB/ $\text{I}_2$  exhibits distinct diffraction peaks at  $7.9^\circ$ ,  $15.8^\circ$ ,  $27.3^\circ$ , and  $30.2^\circ$ , associated with the (100), (200), (300), and (001) crystal planes of Cu-HHB, respectively. This result suggests high structural stability of Cu-HHB upon  $\text{I}_2$  loading. In order to investigate the structural composition and element states of Cu-HHB/ $\text{I}_2$ , X-ray photoelectron spectroscopy (XPS) measurement was conducted. The XPS survey spectrum of Cu-HHB/ $\text{I}_2$  evidences the presence of C, O, Cu, and I elements (Figure S7, Supporting Information). The deconvoluted O 1s XPS spectrum (Figure 1g) can be divided into Cu–O ( $530.8 \text{ eV}$ ), C–O ( $531.9 \text{ eV}$ ), C=O ( $533.1 \text{ eV}$ ), and

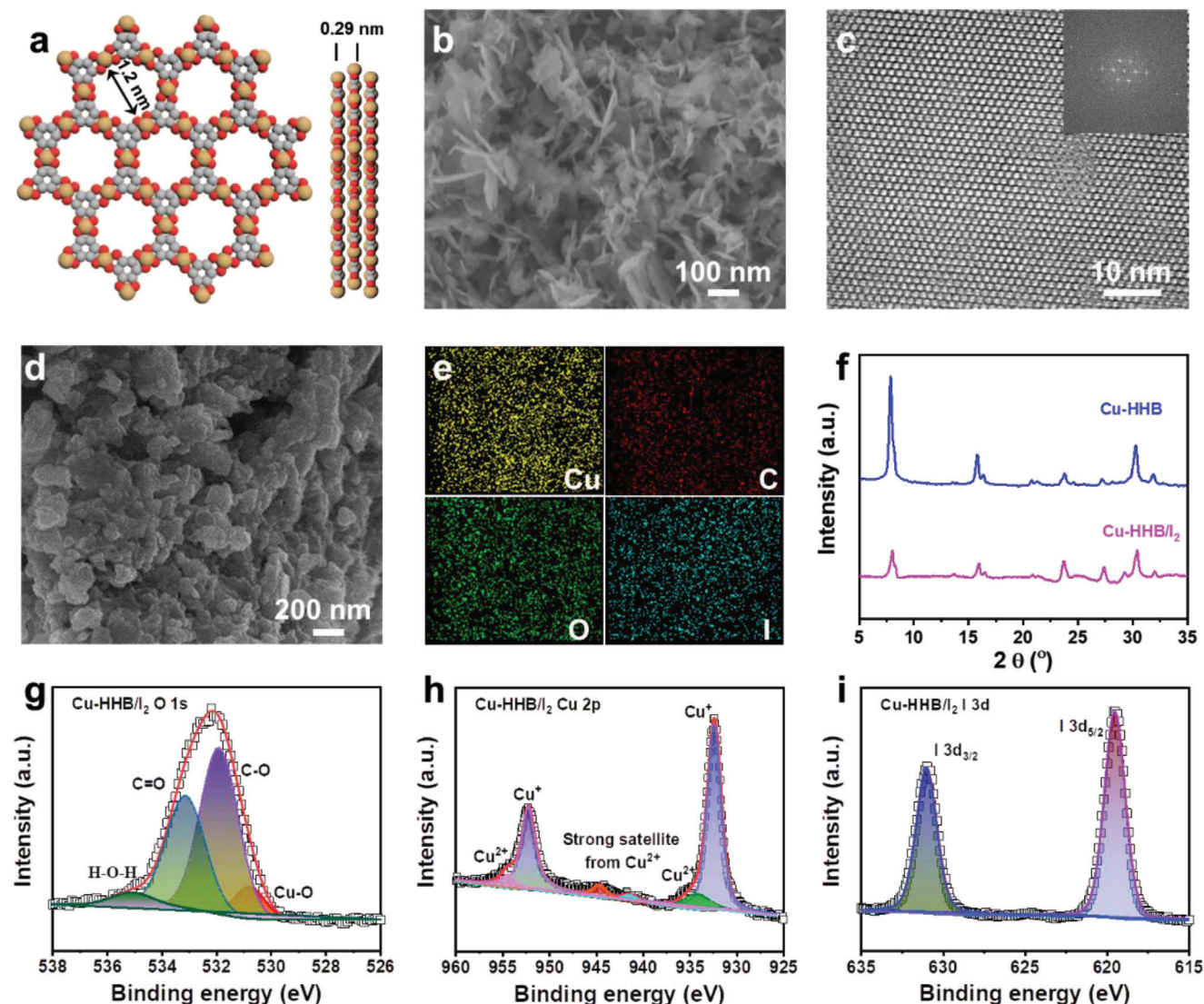


**Figure 1.** Synthesis and characterizations of Cu-HHB and Cu-HHB/I<sub>2</sub>. a) The unit-cell structures of Cu-HHB derived using AB slipped-parallel stacking models. The brown, orange, and gray spheres represent Cu, O, and C atoms, respectively. b) SEM image of Cu-HHB. c) AC-HRTEM image of Cu-HHB. Inset: corresponding FFT image. d,e) SEM image of Cu-HHB/I<sub>2</sub> and corresponding EDX elemental mapping analysis. f) PXRD patterns of Cu-HHB and Cu-HHB/I<sub>2</sub>. g–i) High-resolution XPS spectra of O 1s, Cu 2p, and I 3d for Cu-HHB/I<sub>2</sub>.

H—O—H (535.1 eV).<sup>[16]</sup> The Cu—O peak is indicative of the coordination of C—O and Cu atoms, while the presence of C—O and H—O—H groups is favorable for improving the surface hydrophilicity and electrolyte penetration of Cu-HHB/I<sub>2</sub>. Meanwhile, the high-resolution Cu 2p XPS spectrum (Figure 1h) suggests the oxidation state of Cu<sup>2+</sup>. Notably, the undetected Cu—I and O—I bonds in I 3d XPS spectrum reveal the physical adsorption of I<sub>2</sub> in Cu-HHB/I<sub>2</sub> composite (Figure 1i). Besides, the charge transport property of pelletized Cu-HHB/I<sub>2</sub> was studied using the van-der-Pauw method. The electrical conductivity increases non-linearly ranging from 230 to 310 K, suggesting a typical semi-conducting characteristic (Figures S8 and S9, Supporting Information). Notably, it reaches  $1.44 \times 10^{-5} \text{ S cm}^{-1}$  at 300 K, which is much higher than that of undoped Cu-HHB ( $1.5 \times 10^{-7} \text{ S cm}^{-1}$ ).

Encouraged by the high electrical conductivity, large specific surface area, and rich redox-active sites, Cu-HHB/I<sub>2</sub> composite can be a promising active material for energy storage. Its electrochemical behavior was thus investigated in 1 M (NH<sub>4</sub>)<sub>2</sub>SO<sub>4</sub> electrolyte using a three-electrode system. As shown in Figure 2a, cyclic voltammetry (CV) measurements were first performed to evaluate the electrochemical kinetics. The Cu-HHB electrode shows a nearly rectangular shape with one pair of redox peaks in a potential range of 0 to 0.7 V (vs Ag/AgCl), while broad peaks located at 0.27 and 0.51 V could be attributed to the Cu—O<sub>4</sub> species in Cu-HHB.<sup>[18]</sup> In addition, CV curve of the I<sub>2</sub> electrode exhibits three pairs of distinct redox peaks, ascribed to the conversion reactions of I<sub>2</sub>/I<sub>3</sub><sup>-</sup>, I<sub>2</sub>/I<sup>-</sup>, and I<sub>3</sub><sup>-</sup>/I<sup>-</sup>.<sup>[19]</sup> Interestingly, there is only a slight voltage difference between oxidation and reduction peaks, highlighting the excellent electrochemical

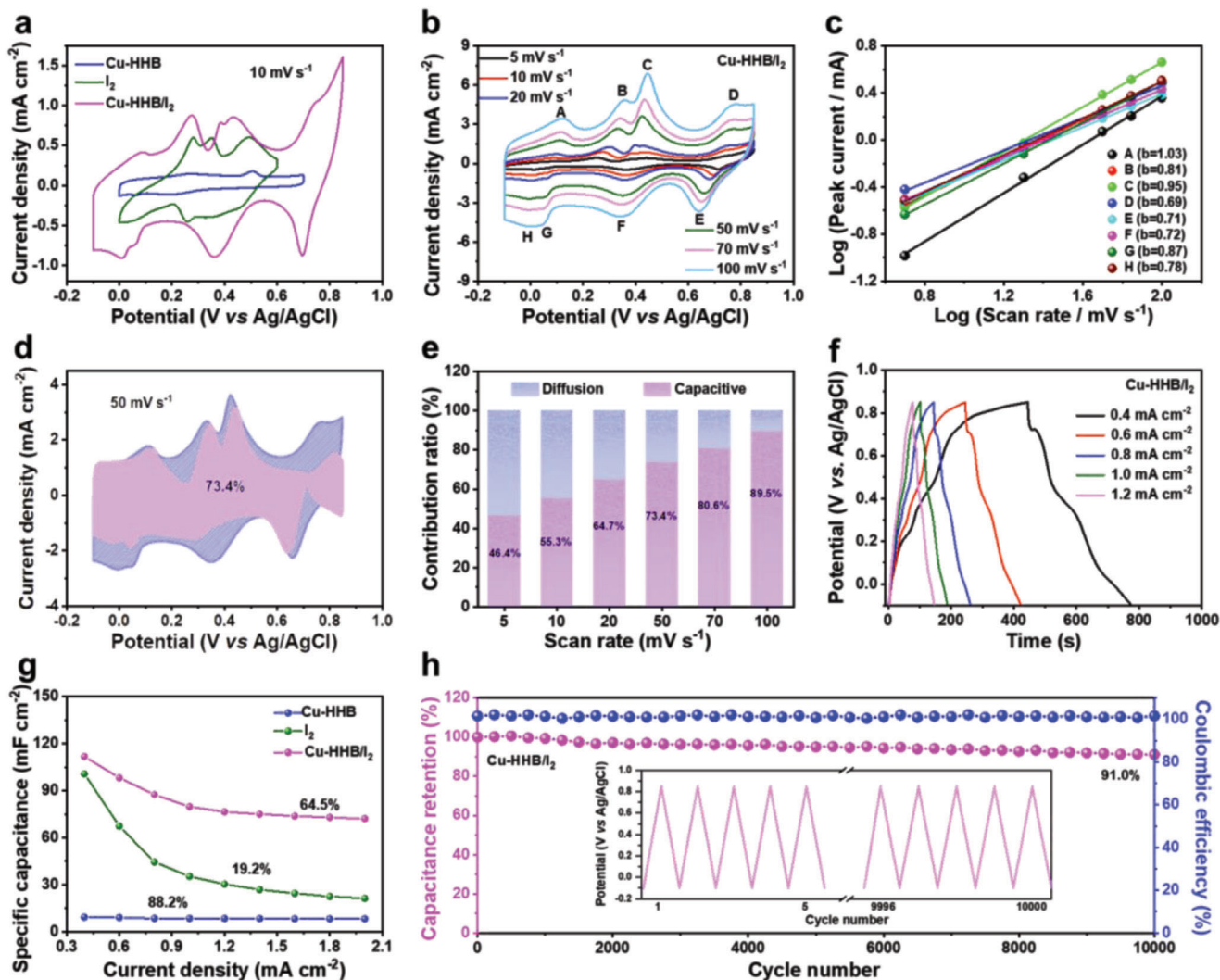


**Figure 2.** Electrochemical performance of the Cu-HHB/ $I_2$  electrode in 1 M  $(NH_4)_2SO_4$  electrolyte. a) CV curves of the Cu-HHB,  $I_2$ , and Cu-HHB/ $I_2$  electrodes at  $10\text{ mV s}^{-1}$ . b) CV curves at scan rates from 5 to  $100\text{ mV s}^{-1}$ . c) Relationship between  $\log(i)$  and  $\log(v)$  from 5 to  $100\text{ mV s}^{-1}$ . d) CV curve of the Cu-HHB/ $I_2$  electrode with separation between the total current and the capacitive (pink) current at  $50\text{ mV s}^{-1}$ . e) Normalized contribution ratios of the capacitive (pink) and diffusion-controlled (blue) currents as a function of scan rate. f) GCD curves at different current densities of 0.4– $1.2\text{ mA cm}^{-2}$ . g) Specific capacitances of the Cu-HHB,  $I_2$ , and Cu-HHB/ $I_2$  electrodes calculated from GCD curves as a function of current density. h) Cycling stability and Coulombic efficiency of the Cu-HHB/ $I_2$  electrode at  $2\text{ mA cm}^{-2}$  for 10 000 cycles. The inset shows the first five and the last five GCD curves.

reversibility of  $I_2$ .<sup>[19b]</sup> By contrast, Cu-HHB/ $I_2$  electrode displays multiple redox peaks with much enhanced current response due to the improved electronic conductivity and high utilization efficiency of  $I_2$ . Based on the CV measurements of the Cu-HHB and  $I_2$  electrodes (Figure S10, Supporting Information), the reduction peaks located at 0.02 and 0.05 V of Cu-HHB/ $I_2$  originate from the contribution of Cu-HHB while the one located at 0.36 V results from the synergistic interaction of Cu-HHB and  $I_2$ . Accordingly, the oxidation peaks at 0.08, 0.28, 0.41, 0.47, and 0.72 V can be ascribed to the redox reactions of Cu-HHB,  $I_2/I_3^-$ , Cu-HHB,  $I_2/I^-$ , and  $I_3^-/I^-$ , respectively. As the scan rates increase from 5 to  $500\text{ mV s}^{-1}$ , the characteristic CV curves remain unchanged, suggesting the fast electrochemical response and excellent redox reversibility of Cu-HHB/ $I_2$  (Figure 2b). To gain more insights into the storage mechanism of Cu-HHB/ $I_2$  in

$NH_4^+$ -containing electrolyte, the  $b$ -values for eight redox peaks (A–H) are calculated according to the following Equations (1) and (2).<sup>[20]</sup>

$$i = av^b \quad (1)$$

$$\log(i) = b\log(v) + \log(a) \quad (2)$$

where  $i$  and  $v$  represent peak current and scan rate respectively,  $a$  is a constant, and  $b$  is derived from the slope of  $\log(i)$  as a function of  $\log(v)$ . The  $b$ -values of 0.5 or 1 represent a diffusion-controlled or surface-controlled process for the redox reaction, respectively.<sup>[21]</sup> As depicted in Figure 2c, the  $b$ -values of 1.03 (peak A), 0.81 (peak B), 0.95 (peak C), 0.87 (peak G), and 0.78 (peak H) indicate a dominant capacitive behavior. While the

*b*-values of 0.69 (peak D), 0.71 (peak E), and 0.72 (peak F) are more intended to be 0.5, suggesting a combined surface capacitive and diffusion-controlled behavior. Generally, the Cu-HHB/I<sub>2</sub> electrode possesses a hybrid mechanism with both capacitive and diffusion effects in NH<sub>4</sub><sup>+</sup>-containing electrolyte. The capacitive and diffusion-controlled contribution ratios are then determined by the following Equation (3).<sup>[17]</sup>

$$i = k_1 v + k_2 v^{1/2} \quad (3)$$

where *i*, *v*, *k*<sub>1</sub>*v*, and *k*<sub>2</sub>*v*<sup>1/2</sup> represent total current, scan rate, capacitive-dominated current, and diffusion-controlled current, respectively. As shown in Figure 2d, the capacitive contribution from the Cu-HHB/I<sub>2</sub> electrode accounts for 73.4% at a scan rate of 50 mV s<sup>-1</sup>. Moreover, by increasing the scan rates from 5 to 100 mV s<sup>-1</sup> (Figure 2e), the capacitive contribution keeps growing and reaches 89.5% at 100 mV s<sup>-1</sup>, endowing the fast electrochemical kinetics at high scan rates.

The galvanostatic charge–discharge (GCD) profiles of the Cu-HHB/I<sub>2</sub> electrode display approximately symmetrical shapes with multiple small plateaus (Figure 2f), in good agreement with the CV redox peaks. In comparison to the GCD curves of the Cu-HHB and I<sub>2</sub> electrodes (Figure S11, Supporting Information), the Cu-HHB/I<sub>2</sub> electrode displays a much longer discharge time, suggesting an enhanced capacitance due to the synergistic effect of two components. According to the GCD curves, the areal capacitance of the Cu-HHB/I<sub>2</sub> electrode reaches 111.7 mF cm<sup>-2</sup> at a current density of 0.4 mA cm<sup>-2</sup> (Figure 2g). As the current density increases to 2 mA cm<sup>-2</sup>, the Cu-HHB/I<sub>2</sub> electrode shows excellent rate capability with capacitance retention of 64.5%. Meanwhile, the Nyquist plots demonstrate a negligible small resistance of the Cu-HHB, I<sub>2</sub>, and Cu-HHB/I<sub>2</sub> electrodes (Figure S12, Supporting Information). Furthermore, the cycling stability of the Cu-HHB/I<sub>2</sub> electrode was evaluated at a current density of 2 mA cm<sup>-2</sup> (Figure 2h). After 10 000 charge/discharge cycles, the areal capacitance maintained 91.0% of its initial capacitance and the Coulombic efficiency presented no noticeable decay, revealing the state-of-the-art cycling performance of the Cu-HHB/I<sub>2</sub> electrode, superior to many currently reported cathode materials for NH<sub>4</sub><sup>+</sup> storage.

To elucidate the storage mechanism of the Cu-HHB/I<sub>2</sub> electrode in aqueous NH<sub>4</sub><sup>+</sup>-containing electrolyte, ex situ XPS was employed to detect the structural changes of Cu-HHB/I<sub>2</sub> at different charge/discharge states (Figure 3a). As illustrated in Figure 3b, the peaks located at 934.6 and 952.1 eV strengthened when charging to 0.15 V, indicating the transition from Cu<sup>+</sup> to Cu<sup>2+</sup> and a redox reaction of Cu–O<sub>4</sub> species.<sup>[16,22]</sup> With charging to 0.55 V, Cu<sup>2+</sup> showed a strong satellite peak, which is attributed to further redox reaction of Cu–O<sub>4</sub> species. In addition, Cu<sup>2+</sup> began to transform to Cu<sup>+</sup> when discharged to 0.2 V. When discharged to the initial voltage, the peaks of Cu<sup>2+</sup> became weaker, and the chemical state of Cu 2p was almost identical to that of the original state, supporting a reversible redox reaction of the Cu–O<sub>4</sub> species. In Figure 3c, the peak of O 1s moved to a lower binding energy, and finally recovered to the original location, indicating a reversible conversion between C=O and C–O groups. This result further confirms that the Cu–O<sub>4</sub> species is the redox-active center of Cu-HHB/I<sub>2</sub>.<sup>[22a,c]</sup> High-resolution spectra of I 3d are shown in Figure 3d, where the peaks of Cu-HHB/I<sub>2</sub> in the

pristine state located at 631.1 and 619.7 eV are indexed to I 3d<sub>3/2</sub> and I 3d<sub>5/2</sub>.<sup>[23]</sup> As charging to 0.18 V, the peaks shifted to a lower binding energy, implying a lower oxidation state.<sup>[24]</sup> With further charging to 0.3 V, the iodide underwent redox reaction, causing shift to the left peak. When fully charging to 0.85 V, these peaks shifted to the original positions, indicating oxidation of I<sup>-</sup> back to elemental I<sup>0</sup>. The entire I 3d spectrum shifted to a lower binding energy when the Cu-HHB/I<sub>2</sub> was discharged, revealing the reduction of iodine.<sup>[24]</sup> At a fully discharged state of –0.1 V, the peaks are distributed at 630.8 and 619.4 eV. Taking the high-resolution spectra of Cu 2p, O 1s, and I 3d into full consideration, the absence of Cu–I and I–O bonds demonstrates the physical adsorption of iodine in Cu-HHB/I<sub>2</sub>.

The excellent cycling performance of the Cu-HHB/I<sub>2</sub> electrode indicates limited dissolution of iodine, iodide, and polyiodide ions in the aqueous electrolytes upon cycling. DFT theoretical calculations on the possible iodide adsorption sites at Cu-HHB were performed by simulating the molecular electrostatic potential (MSEP).<sup>[25]</sup> The red and blue electron density equivalence surfaces represent the positive and negative electrostatic potentials, respectively (Figure 3e). The red atomic density cloud in the center of Cu sites indicates the most electropositive of Cu sites, which contribute to the adsorption of iodide. Further comparison of different sites for iodide adsorption energy in Cu-HHB is presented in Figures 3f–i. The simulated maximum adsorption energy of iodide on site 1, site 2, site 3, and site 4. Remarkably, the solvent energy of iodine in water is only 0.30 eV (Figure S13, Supporting Information). The good anchoring effect on iodide of Cu sites effectively inhibits the diffusion of iodine in aqueous NH<sub>4</sub><sup>+</sup> electrolyte. Combined with electrochemical results, the charge-storage process of Cu-HHB/I<sub>2</sub> involves the redox reactions of both Cu–O<sub>4</sub> species and iodide adsorbed on Cu sites in Cu-HHB. Compared to pristine Cu-HHB and I<sub>2</sub>, Cu-HHB/I<sub>2</sub> exhibits much higher pseudocapacitance due to the synergistic effect. Based on the electrochemical performance of the Cu-HHB, I<sub>2</sub>, and Cu-HHB/I<sub>2</sub> electrodes, the capacitive contributions of Cu–O<sub>4</sub> and I<sub>2</sub> to Cu-HHB/I<sub>2</sub> were estimated to be 26.4% and 73.6%, respectively.

To further evaluate the practical potential of Cu-HHB/I<sub>2</sub>, porous MXene (P-MXene) synthesized by fluoride-based salt etching strategy and sulfur-template method was chosen as the coupled anode material. As shown in Figure 4a and Figure S14, Supporting Information, Ti<sub>3</sub>C<sub>2</sub>T<sub>x</sub> dispersions with different concentrations were obtained by LiF/HCl chemical etching of the Ti<sub>3</sub>AlC<sub>2</sub> precursor and subsequent delamination in deionized water. As characterized by SEM, TEM, and XRD (Figures S15–S17, Supporting Information), the synthesized micrometer-scale Ti<sub>3</sub>C<sub>2</sub>T<sub>x</sub> sheets show irregular edges and high quality. The P-MXene films with good flexibility were further prepared by vacuum-filtrating Ti<sub>3</sub>C<sub>2</sub>T<sub>x</sub> dispersion mixed with sulfur spheres and annealed at high temperature (400 °C, Figures S18 and S19, Supporting Information). The XRD patterns (Figure 4b) and SEM images (Figure S20, Supporting Information) demonstrate that the optimal mass ratio of sulfur to MXene was 1:4 in the fabricated P-MXene films. As depicted in Figure 4c, the obtained P-MXene film was fluffy with hierarchical porous structure. Figure 4d evidences the multigradient pore sizes, which are beneficial to the

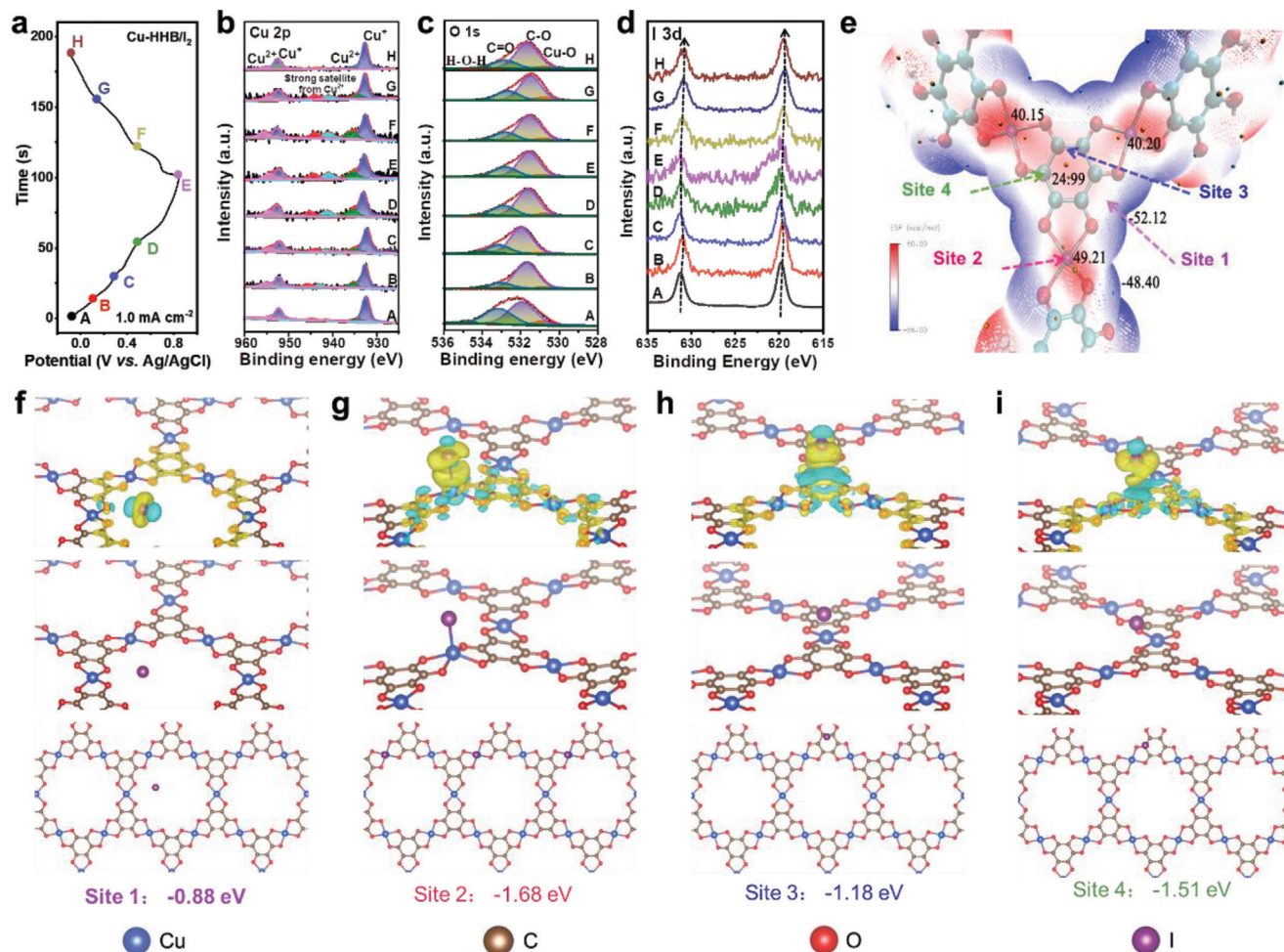


**Figure 3.** Charge-storage mechanism of Cu-HHB/I<sub>2</sub>. a) GCD curve of the Cu-HHB/I<sub>2</sub> electrode at a current density of 1.0 mA cm<sup>-2</sup> and b–d) corresponding ex situ Cu 2p (b), O 1s (c), and I 3d (d) XPS spectra of the Cu-HHB/I<sub>2</sub> electrode at different charge/discharge potentials. e) Calculated MESP distribution of Cu-HHB. f–i) The comparison of optimized different sites for iodide adsorption energy in Cu-HHB.

rapid ion diffusion of the electrolyte. Besides, XPS spectra reveal the multivalence states of Ti and the sulfur doping during the template removal (Figure 4e and Figure S21, Supporting Information).<sup>[26]</sup>

As a freestanding film electrode, the P-MXene shows the CV curves at different scan rates with nearly rectangular shapes (Figure 4f), indicating fast electrochemical reaction kinetics originated from the hierarchical porous structure and metallic conductivity of MXene (Figure S22, Supporting Information). These electrochemical results indicate the capacitive behavior of the P-MXene electrode in 1 M (NH<sub>4</sub>)<sub>2</sub>SO<sub>4</sub> electrolyte (Figure S23, Supporting Information), in good agreement with other literature.<sup>[14,27]</sup> NH<sub>4</sub><sup>+</sup> ions can be stored on the surface of P-MXene nanosheets and intercalated between P-MXene layers. Moreover, the excellent reversible stability of the P-MXene electrode is demonstrated by the GCD curves, which exhibit superior symmetry (Figure 4g). The P-MXene electrode presents an areal capacitance of 240 mF cm<sup>-2</sup> at a current density of 0.4 mA cm<sup>-2</sup> (Figure 4h). Even at a high current density of 2 mA cm<sup>-2</sup>, the areal capacitance still preserves 80.0%. In addition, the capacitance retention of 88.7% together with the Coulombic efficiency of

nearly 100% are achieved after 10 000 charge/discharge cycles at 2 mA cm<sup>-2</sup> (Figure 4i).

Finally, an NH<sub>4</sub><sup>+</sup> HSC (Cu-HHB/I<sub>2</sub>//P-MXene) was assembled with Cu-HHB/I<sub>2</sub> cathode and P-MXene anode in 1 M (NH<sub>4</sub>)<sub>2</sub>SO<sub>4</sub> electrolyte, as illustrated in Figure 5a. According to the potential windows of the Cu-HHB/I<sub>2</sub> electrode (−0.1–0.85 V) and the P-MXene electrode (−0.75 to 0.1 V), a maximum voltage range of 0–1.6 V can be achieved for Cu-HHB/I<sub>2</sub>//P-MXene NH<sub>4</sub><sup>+</sup> HSCs (Figure 5b). In order to reach the charge balance between Cu-HHB/I<sub>2</sub> cathode and P-MXene anode, the ideal mass ratio of cathode to anode was determined to be 1.7. Figure 5c shows the CV curves of Cu-HHB/I<sub>2</sub>//P-MXene NH<sub>4</sub><sup>+</sup> HSCs at scan rates of 5–100 mV s<sup>-1</sup>, which display several pairs of redox peaks with multielectron transfer. Even at high scan rates, there is no obvious polarization up to 1.6 V, indicating a good electrochemical reversibility of Cu-HHB/I<sub>2</sub>//P-MXene NH<sub>4</sub><sup>+</sup> HSCs. In addition, the apparent plateaus in GCD profiles from 0.4 to 2.0 mA cm<sup>-2</sup> correspond well with the CV curves (Figure 5d). At a current density of 0.4 mA cm<sup>-2</sup>, Cu-HHB/I<sub>2</sub>//P-MXene NH<sub>4</sub><sup>+</sup> HSCs achieve a high areal capacitance of 88.5 mF cm<sup>-2</sup>. Moreover, when increasing the current density to 2 mA cm<sup>-2</sup>, the

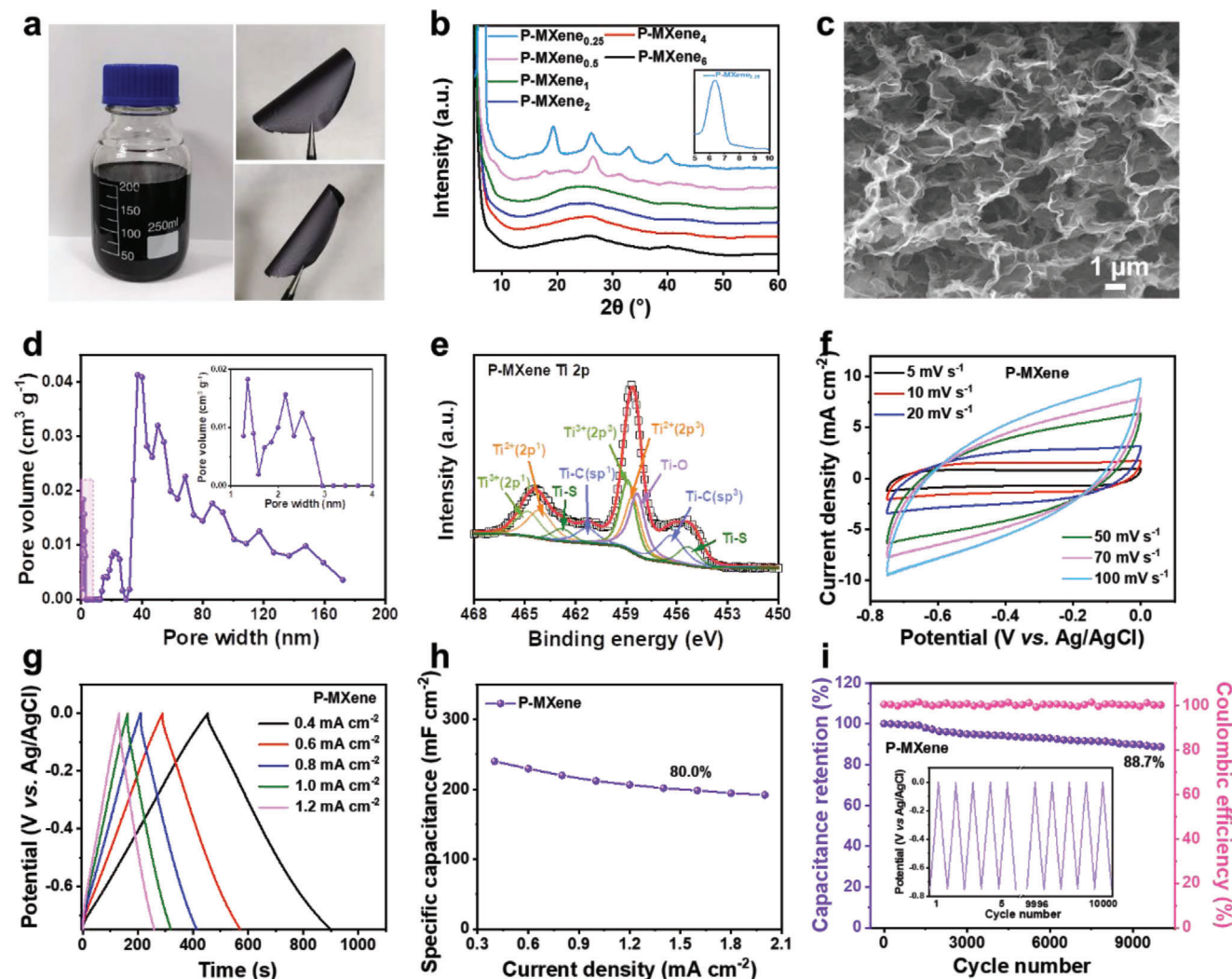


**Figure 4.** Structural characterizations and electrochemical performance of P-MXene. a) Digital photographs of MXene dispersion and P-MXene films. b) XRD patterns. c) SEM image. d) Pore size distribution. e) Ti 2p XPS spectra. f) CV curves at scan rates ranging from 5 to 100  $\text{mV s}^{-1}$ . g) GCD curves at different current densities of 0.4–1.2  $\text{mA cm}^{-2}$ . h) Specific capacitances calculated from different current densities. i) Cycling stability and Coulombic efficiency of the P-MXene electrode at 2  $\text{mA cm}^{-2}$  for 10 000 cycles. The inset shows the first five and the last five GCD curves.

fabricated  $\text{NH}_4^+$  HSCs display a good rate capability with capacitance retention of 67.1% (Figure 5e). Furthermore, only a small semicircle was observed in the high-frequency region of the Nyquist plot (Figure 5f), indicating fast ion diffusion and rapid charge transfer. Note that the open porosity and thin-sheet morphology of Cu-HHB likely lead to  $\text{NH}_4^+$  ion diffusion predominating along the pore channels as the primary pathway for  $\text{NH}_4^+$  insertion, rather than diffusion between the layers. To evaluate the overall performance of Cu-HHB/ $\text{I}_2$ //P-MXene  $\text{NH}_4^+$  HSCs, Figure 5g summarizes the Ragone plots in comparison with the state-of-the-art HSCs. A maximal energy density of 31.5  $\text{mWh cm}^{-2}$  is obtained at a power density of 400  $\text{mW cm}^{-2}$ , superior to those of the state-of-the-art  $\text{NH}_4^+$  HSCs.<sup>[2a,4b,10a,28]</sup> The full device still delivers an energy density of 21.1  $\text{mWh cm}^{-2}$  even at a power density of 2000  $\text{mW cm}^{-2}$ . Compared with other previously reported SCs (Table S1, Supporting Information), such as  $\text{MnO}_2/\text{CNTF}/\text{MoS}_2@\text{TiN}/\text{CNTF}$  (195.1  $\mu\text{Wh cm}^{-2}$

at 1.1  $\text{mW cm}^{-2}$ ),<sup>[2a]</sup>  $\alpha\text{-MnO}_2/((\text{NH}_4)_x\text{WO}_3$  (1010.1  $\mu\text{Wh cm}^{-2}$  at 18.0  $\text{mW cm}^{-2}$ ),<sup>[10a]</sup>  $\delta\text{-MnO}_2/\text{ACC}$  (861.2  $\mu\text{Wh cm}^{-2}$  at 20.0  $\text{mW cm}^{-2}$ ),<sup>[4b]</sup>  $\text{ACC@VPP}/\text{PTCDI}$  (320  $\mu\text{Wh cm}^{-2}$  at 0.09  $\text{mW cm}^{-2}$ ),<sup>[28]</sup>  $\text{Co-Al LDH}/\text{Ti}_3\text{C}_2\text{T}_x$  (10.8  $\mu\text{Wh cm}^{-2}$  at 0.37  $\text{mW cm}^{-2}$ ),<sup>[29]</sup> and  $\text{Ti}_3\text{C}_2\text{T}_x/\text{CNF}/\text{Ti}_3\text{C}_2\text{T}_x/\text{CNF}$  (101  $\mu\text{Wh cm}^{-2}$  at 0.299  $\text{mW cm}^{-2}$ ),<sup>[30]</sup> the Cu-HHB/ $\text{I}_2$ //P-MXene  $\text{NH}_4^+$  HSCs show superior energy and power characteristics. The long-term cycling stability test was conducted at a current density of 2  $\text{mA cm}^{-2}$ . Notably, the Cu-HHB/ $\text{I}_2$ //P-MXene  $\text{NH}_4^+$  HSCs exhibit outstanding capacitance retention of 89.5% after 10 000 cycles and the Coulombic efficiency maintains almost 100% during the cycling test (Figure 5h).

### 3. Conclusion

We have demonstrated a large pseudocapacitive Cu-HHB/ $\text{I}_2$  cathode material for high-performance  $\text{NH}_4^+$  HSCs.

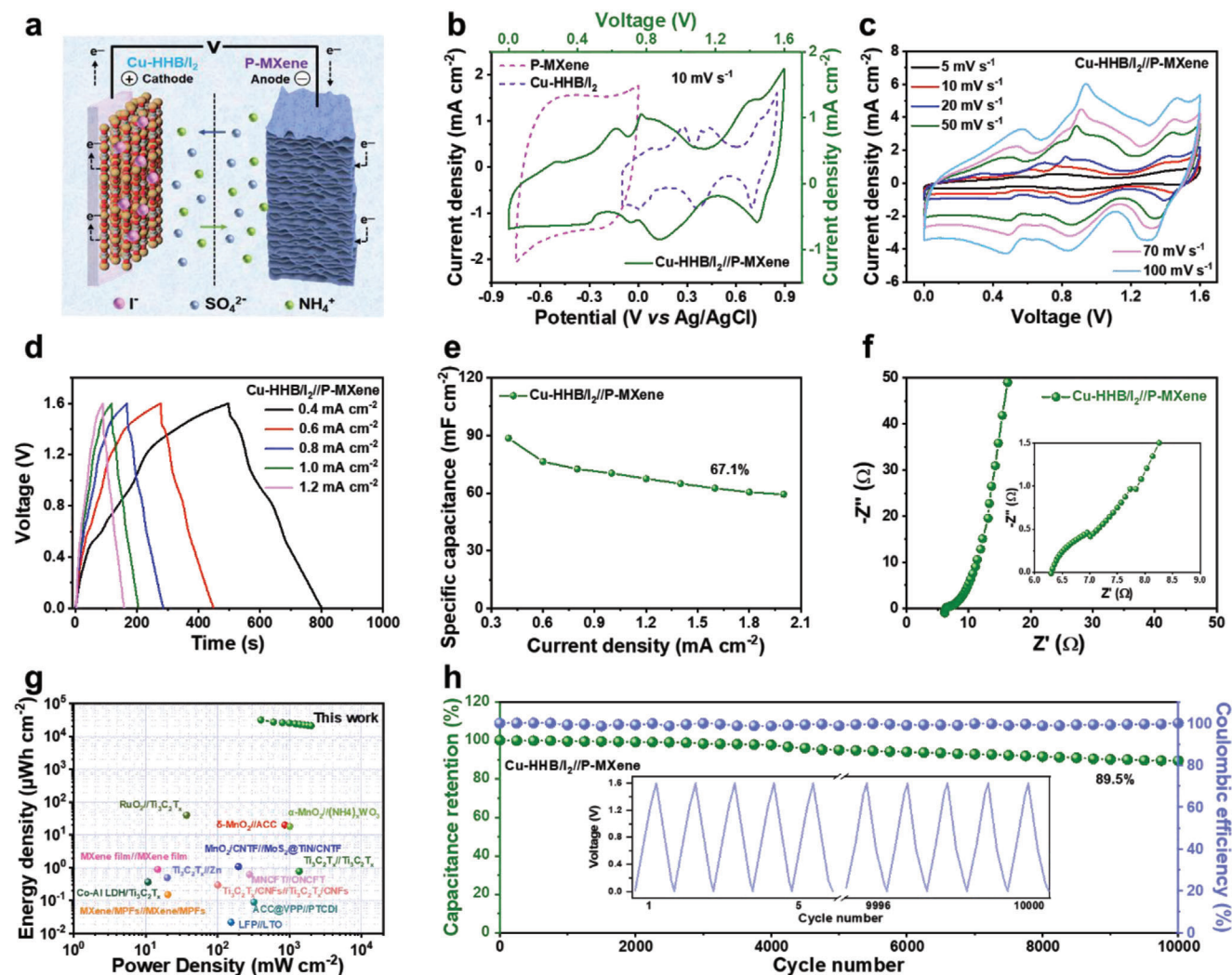


**Figure 5.** Electrochemical performance of Cu-HHB/I<sub>2</sub>//P-MXene NH<sub>4</sub><sup>+</sup> HSCs. a) Schematic illustration of the Cu-HHB/I<sub>2</sub>//P-MXene NH<sub>4</sub><sup>+</sup> HSCs. b) CV curves of Cu-HHB/I<sub>2</sub> cathode, P-MXene anode, and Cu-HHB/I<sub>2</sub>//P-MXene NH<sub>4</sub><sup>+</sup> HSC at 10 mV s<sup>-1</sup>. c) CV curves at different scan rates of 5–100 mV s<sup>-1</sup>. d) GCD curves at different current densities of 0.4–1.2 mA cm<sup>-2</sup>. e) Specific capacitances calculated from different current densities. f) Nyquist plots. g) Ragone plots of Cu-HHB/I<sub>2</sub>//P-MXene NH<sub>4</sub><sup>+</sup> HSCs in comparison with other reported HSCs. h) Cycling stability and Coulombic efficiency of Cu-HHB/I<sub>2</sub>//P-MXene NH<sub>4</sub><sup>+</sup> HSCs at 2 mA cm<sup>-2</sup> for 10 000 cycles. The inset shows the first five and the last five GCD curves.

Electrochemical analyses combined with DFT calculations reveal that the outstanding performance of the Cu-HHB/I<sub>2</sub> electrode originates from the multielectron Faradaic reactions of Cu–O<sub>4</sub> species in Cu-HHB and the presence of electroactive I<sub>2</sub>. By pairing the Cu-HHB/I<sub>2</sub> cathode with the P-MXene anode, the resulting NH<sub>4</sub><sup>+</sup> HSCs exhibit an ultrahigh areal energy density (31.5 mWh cm<sup>-2</sup> at 400 mW cm<sup>-2</sup>) and excellent long-term cycling stability (89.5% after 10 000 cycles). The fabricated Cu-HHB/I<sub>2</sub> could be promising in various applications such as optoelectronics, metal-iodine batteries, sensing, and catalysis. Moreover, this work demonstrates the viability of MOF-based materials for NH<sub>4</sub><sup>+</sup> energy storage and presents a noteworthy case for porous nanomaterials functionalized with small molecules. This study offers a new avenue for the design of highly electroactive framework cathode materials toward non-metallic ion storage, and highlights an efficient strategy for developing advanced hybrid energy devices.

## Supporting Information

Supporting Information is available from the Wiley Online Library or from the author.

## Acknowledgements

M.G. and Z.W. contributed equally to this work. This work was financially supported by the National Natural Science Foundation of China (22209051), the Science Foundation of Huazhong University of Science and Technology (3034110102), the Hubei Provincial Natural Science Foundation of China (2021CFA020), the National Science Foundation of China (no. 21925104), the EU Graphene Flagship (Core3, no. 881603), the ERC Starting Grant (FC2DMOF, no. 852909), the ERC Consolidator Grant (T2DCP), and the DFG projects (SFB-1415, no. 417590517, SPP 1928, COORNET). Z.L. acknowledges support from the China Postdoctoral Science Foundation (2023M730562) and the Jiangsu Funding Program for Excellent Postdoctoral Talent (2023ZB187). The authors acknowledge the



use of the facilities at the Analytical and Testing Center in Huazhong University of Science and Technology.

Open access funding enabled and organized by Projekt DEAL.

## Conflict of Interest

The authors declare no conflict of interest.

## Data Availability Statement

The data that support the findings of this study are available from the corresponding author upon reasonable request.

## Keywords

2D conjugated metal–organic frameworks, cathode, hybrid supercapacitors,  $I_2$ ,  $NH_4^+$

Received: June 10, 2023

Revised: August 16, 2023

Published online: August 30, 2023

- [1] a) X. Li, Y. Tang, J. Zhu, H. Lv, Y. Xu, W. Wang, C. Zhi, H. Li, *Adv. Energy Mater.* **2021**, *11*, 2003714; b) D. Chao, H. J. Fan, *Chem* **2019**, *5*, 1359; c) L. Niu, T. Wu, M. Chen, L. Yang, J. Yang, Z. Wang, A. A. Kornyshev, H. Jiang, S. Bi, G. Feng, *Adv. Mater.* **2022**, *34*, 2200999.
- [2] a) L. Han, J. Luo, R. Zhang, W. Gong, L. Chen, F. Liu, Y. Ling, Y. Dong, Z. Yong, Y. Zhang, L. Wei, X. Zhang, Q. Zhang, Q. Li, *ACS Nano* **2022**, *16*, 14951; b) Z. Xiong, P. Guo, Y. Yang, S. Yuan, N. Shang, C. Wang, Y. Zhang, H. Wang, Y. Gao, *Adv. Energy Mater.* **2022**, *12*, 2103226; c) M. S. Javed, X. Zhang, S. Ali, A. Mateen, M. Idrees, M. Sajjad, S. Batool, A. Ahmad, M. Imran, T. Najam, W. Han, *Nano Energy* **2022**, *101*, 107624; d) F. Xing, Z. Bi, F. Su, F. Liu, Z.-S. Wu, *Adv. Energy Mater.* **2022**, *12*, 2200594.
- [3] a) Y. Wang, R. Chen, T. Chen, H. Lv, G. Zhu, L. Ma, C. Wang, Z. Jin, J. Liu, *Energy Storage Mater.* **2016**, *4*, 103; b) X. Ji, *Energy Environ. Sci.* **2019**, *12*, 3203; c) S. Wang, T. Li, Y. Yin, N. Chang, H. Zhang, X. Li, *Nano Energy* **2022**, *96*, 107120; d) F. Su, J. Qin, P. Das, F. Zhou, Z.-S. Wu, *Energy Environ. Sci.* **2021**, *14*, 2269; e) H. Y. Ma, H. W. Chen, Y. J. Hu, B. J. Yang, J. Z. Feng, Y. T. Xu, Y. L. Sun, H. H. Cheng, C. Li, X. B. Yan, L. T. Qu, *Energy Environ. Sci.* **2022**, *15*, 1131.
- [4] a) A. W. Xiao, G. Galatolo, M. Pasta, *Joule* **2021**, *5*, 2823; b) Q. Chen, J. Jin, M. Song, X. Zhang, H. Li, J. Zhang, G. Hou, Y. Tang, L. Mai, L. Zhou, *Adv. Mater.* **2022**, *34*, 2107992.
- [5] a) J. Han, A. Varzi, S. Passerini, *Angew. Chem., Int. Ed.* **2022**, *61*, e202115046; b) Y.-Z. Zhang, J. Liang, Z. Huang, Q. Wang, G. Zhu, S. Dong, H. Liang, X. Dong, *Adv. Sci.* **2022**, *9*, 2105158; c) M. Zhu, L. Zhao, Q. Ran, Y. Zhang, R. Peng, G. Lu, X. Jia, D. Chao, C. Wang, *Adv. Sci.* **2022**, *9*, 2103896; d) G. Liang, Y. Wang, Z. Huang, F. Mo, X. Li, Q. Yang, D. Wang, H. Li, S. Chen, C. Zhi, *Adv. Mater.* **2020**, *32*, 1907802; e) R. Zhang, S. Wang, S. Chou, H. Jin, *Adv. Funct. Mater.* **2022**, *32*, 2112179; f) X. Wu, Y. Qi, J. J. Hong, Z. Li, A. S. Hernandez, X. Ji, *Angew. Chem., Int. Ed.* **2017**, *56*, 13026.
- [6] Y. Song, Q. Pan, H. Lv, D. Yang, Z. Qin, M. Y. Zhang, X. Sun, X. X. Liu, *Angew. Chem., Int. Ed.* **2021**, *60*, 5718.
- [7] a) H. Zhang, Y. Tian, W. Wang, Z. Jian, W. Chen, *Angew. Chem., Int. Ed.* **2022**, *134*, e202204351; b) J. Han, M. Zarrabeitia, A. Mariani, M. Kuenzel, A. Mullaliu, A. Varzi, S. Passerini, *Adv. Mater.* **2022**, *34*, 2201877; c) J. Dai, X. Qi, L. Xia, Q. Xue, L. Luo, X. Wang, C. Yang, D. Li, H. Xie, A. Cabot, L. Dai, Y. Xu, *Adv. Funct. Mater.* **2023**, *33*, 2212440.
- [8] a) X. Zhang, M. Xia, H. Yu, J. Zhang, Z. Yang, L. Zhang, J. Shu, *Nano-Micro Lett.* **2021**, *13*, 139; b) L. Chen, W. Sun, K. Xu, Q. Dong, L. Zheng, J. Wang, D. Lu, Y. Shen, J. Zhang, F. Fu, H. Kong, J. Qin, H. Chen, *ACS Energy Lett.* **2022**, *7*, 1672; c) Z. Zhao, W. Zhang, M. Liu, S. J. Yoo, N. Yue, F. Liu, X. Zhou, K. Song, J.-G. Kim, Z. Chen, X.-Y. Lang, Q. Jiang, C. Zhi, W. Zheng, *Nano Lett.* **2023**, *23*, 5307; d) L. Yan, Y.-E. Qi, X. Dong, Y. Wang, Y. Xia, *eScience* **2021**, *1*, 212.
- [9] a) H. Li, J. Yang, J. Cheng, T. He, B. Wang, *Nano Energy* **2020**, *68*, 104369; b) S. Dong, W. Shin, H. Jiang, X. Wu, Z. Li, J. Holoubek, W. F. Stickle, B. Key, C. Liu, J. Lu, P. A. Greaney, X. Zhang, X. Ji, *Chem* **2019**, *5*, 1537.
- [10] a) Q. Chen, M. Song, X. Zhang, J. Zhang, G. Hou, Y. Tang, *J. Mater. Chem. A* **2022**, *10*, 15614; b) S. Wang, Z. Yuan, X. Zhang, S. Bi, Z. Zhou, J. Tian, Q. Zhang, Z. Niu, *Angew. Chem., Int. Ed.* **2021**, *60*, 7056; c) T.-H. Lu, C. Zeng, H. Zhang, X. Shi, Y. Yu, X. Lu, *Small* **2023**, *19*, 2206727.
- [11] J. Dai, C. Yang, Y. Xu, X. Wang, S. Yang, D. Li, L. Luo, L. Xia, J. Li, X. Qi, A. Cabot, L. Dai, *Adv. Mater.* **2023**, *35*, 2303732.
- [12] a) Y. Zhang, Y. An, B. Yin, J. Jiang, S. Dong, H. Dou, X. Zhang, *J. Mater. Chem. A* **2019**, *7*, 11314; b) X. Mu, Y. Song, Z. Qin, J. Meng, Z. Wang, X.-X. Liu, *Chem. Eng. J.* **2023**, *453*, 139575; c) Z. Tian, V. S. Kale, Y. Wang, S. Kandambeth, J. Czaban-Jozwiak, O. Shekhah, M. Eddaoudi, H. N. Alshareef, *J. Am. Chem. Soc.* **2021**, *143*, 19178.
- [13] C. D. Wessells, S. V. Peddada, M. T. Mcdowell, R. A. Huggins, Y. Cui, *J. Electrochem. Soc.* **2011**, *159*, A98.
- [14] M. R. Lukatskaya, O. Mashtalir, C. E. Ren, Y. Dall'agnese, P. Rozier, P. L. Taberna, M. Naguib, P. Simon, M. W. Barsoum, Y. Gogotsi, *Science* **2013**, *341*, 1502.
- [15] a) Q. Liu, F. Ye, K. Guan, Y. Yang, H. Dong, Y. Wu, Z. Tang, L. Hu, *Adv. Energy Mater.* **2023**, *13*, 2202908; b) X. Zhang, H. Wei, B. Ren, J. Jiang, G. Qu, J. Yang, G. Chen, H. Li, C. Zhi, Z. Liu, *Adv. Mater.* **2023**, *35*, 2304209.
- [16] Z. Wang, G. Wang, H. Qi, M. Wang, M. Wang, S. Park, H. Wang, M. Yu, U. Kaiser, A. Fery, S. Zhou, R. Dong, X. Feng, *Chem. Sci.* **2020**, *11*, 7665.
- [17] F. Wang, Z. Liu, C. Yang, H. Zhong, G. Nam, P. Zhang, R. Dong, Y. Wu, J. Cho, J. Zhang, X. Feng, *Adv. Mater.* **2020**, *32*, 1905361.
- [18] P. Zhang, M. Wang, Y. Liu, S. Yang, F. Wang, Y. Li, G. Chen, Z. Li, G. Wang, M. Zhu, R. Dong, M. Yu, O. G. Schmidt, X. Feng, *J. Am. Chem. Soc.* **2021**, *143*, 10168.
- [19] a) F. Wang, J. Tseng, Z. Liu, P. Zhang, G. Wang, G. Chen, W. Wu, M. Yu, Y. Wu, X. Feng, *Adv. Mater.* **2020**, *32*, 2000287; b) L. Ma, Y. Ying, S. Chen, Z. Huang, X. Li, H. Huang, C. Zhi, *Angew. Chem., Int. Ed.* **2021**, *60*, 3791.
- [20] a) Y. An, Y. Tian, C. Liu, S. Xiong, J. Feng, Y. Qian, *ACS Nano* **2021**, *15*, 15259; b) T. Sun, H. Du, S. Zheng, J. Shi, Z. Tao, *Adv. Funct. Mater.* **2021**, *31*, 2010127.
- [21] Z. Su, W. Ren, H. Guo, X. Peng, X. Chen, C. Zhao, *Adv. Funct. Mater.* **2020**, *30*, 2005477.
- [22] a) Y. Wang, J. Song, W. Y. R. Wong, *Angew. Chem., Int. Ed.* **2023**, *62*, e202218343; b) Y. Chen, Q. Zhu, K. Fan, Y. Gu, M. Sun, Z. Li, C. Zhang, Y. Wu, Q. Wang, S. Xu, J. Ma, C. Wang, W. Hu, *Angew. Chem., Int. Ed.* **2021**, *60*, 18769; c) Q. Jiang, P. Xiong, J. Liu, Z. Xie, Q. Wang, X. Q. Yang, E. Hu, Y. Cao, J. Sun, Y. Xu, L. Chen, *Angew. Chem., Int. Ed.* **2020**, *59*, 5273.
- [23] P. Li, X. Li, Y. Guo, C. Li, Y. Hou, H. Cui, R. Zhang, Z. Huang, Y. Zhao, Q. Li, B. Dong, C. Zhi, *Adv. Energy Mater.* **2022**, *12*, 2103648.
- [24] a) C. Guo, B. Han, W. Sun, Y. Cao, Y. Zhang, Y. Wang, *Angew. Chem., Int. Ed.* **2022**, *61*, e202213276; b) C. Xie, Y. Liu, W. Lu, H. Zhang, X. Li, *Energy Environ. Sci.* **2019**, *12*, 1834.
- [25] a) Z. Yang, C. Xu, H. Yan, Y. Liu, C. Yue, L. Zhang, M. Shui, F. Hu, J. Shu, *Adv. Funct. Mater.* **2021**, *31*, 2103893; b) F. Yue, Z. Tie, S. Deng, S. Wang, M. Yang, Z. Niu, *Angew. Chem., Int. Ed.* **2021**, *60*, 13882.

- [26] a) Q. Zhao, Q. Zhu, J. Miao, P. Zhang, P. Wan, L. He, B. Xu, *Small* **2019**, *15*, 1904293; b) M. Shi, R. Wang, L. Li, N. Chen, P. Xiao, C. Yan, X. Yan, *Adv. Funct. Mater.* **2023**, *33*, 2209777.
- [27] a) J. Pang, B. Chang, H. Liu, W. Zhou, *ACS Energy Lett.* **2022**, *7*, 78; b) H. Wang, Y. Wu, X. Yuan, G. Zeng, J. Zhou, X. Wang, J. W. Chew, *Adv. Mater.* **2018**, *30*, 1704561.
- [28] X. Chen, P. Wang, Z. Feng, C. Meng, Y. Zhang, *Chem. Eng. J.* **2022**, *445*, 136747.
- [29] S. Xu, Y. Dall'agnese, G. Wei, C. Zhang, Y. Gogotsi, W. Han, *Nano Energy* **2018**, *50*, 479.
- [30] G. Zhou, M. C. Li, C. Liu, Q. Wu, C. Mei, *Adv. Funct. Mater.* **2021**, *32*, 2109593.